

Hardness-dependent quantum adiabatic schedules for the maximum-independent-set problem

Sébastien Perseguers *

Gradiom Sàrl, Avenue de Tivoli 4, 1700 Fribourg, Switzerland

(Dated: June 10, 2025)

We propose a numerical approach to design highly efficient adiabatic schedules for analog quantum computing, focusing on the maximum-independent-set problem and neutral atom platforms. On the basis of a representative dataset of small graphs, we present numerical evidence that the optimum schedules depend principally on the hardness of the problem rather than on its size. These schedules perform better than the benchmark protocols and admit a straightforward implementation in the hardware. This allows us to extrapolate the results to larger graphs and to successfully solve moderately hard problems using QuEra's 256-qubit Aquila computer. We believe that extending our approach to hybrid algorithms could be the key to solving the hardest instances with the current technology, making yet another step toward real-world applications.

I. INTRODUCTION

In recent years, quantum computers have emerged as a promising way to solve complex optimization tasks in science and industry, notably those based on combinatorics where an exhaustive search is not tractable [1–3]. Typically, the problem of interest is encoded in the ground state of a quantum Hamiltonian, which can be reached through adiabatic evolution starting from an easy-to-prepare initial state [4–7]. Advanced protocols have to be developed to overcome not only the hardware limitations, such as qubit decoherence and control errors, but also the intrinsic complication of a vanishing gap in the eigenspectrum during the adiabatic evolution [8–11].

Here we focus on the maximum-independent-set (MIS) problem, where the goal is to find the largest set of vertices that do not share an edge in a graph. Such problems appear naturally in practical applications, for instance, network design [12] or financial analysis [13], and are known to be NP-hard in general [14]. Finding a MIS is still a difficult task in the particular case of unit disk graphs, in which any two vertices are connected by an edge if they are closer than a fixed distance [15, 16]. This family of graphs admits a direct mapping to arrays of Rydberg atoms, which explains the popularity of the MIS problem in analog quantum computing [17–23]. In that setting, optical tweezers enable arbitrary arrangements of atoms and controlled laser pulses manipulate the quantum states [24, 25]. The lasers then drive the evolution of the system according to schedules that are specific to the problem to be solved.

The precise description of the schedules is of utmost importance since it conditions the success of the quantum algorithm. Many methods based on adiabatic criteria or on carefully chosen ansatzes can be applied in this case: quantum approximate optimization algorithm and variational quantum eigensolver [26–28], shortcut to

adiabaticity and counteradiabatic (CD) protocol [29–32], Bayesian and recursive optimization [33, 34], machine learning [35], and variational sampler [36], to name a few. Most of the aforementioned methods require multiple iterations to be run on a quantum device and to be updated by a classical optimizer and thus belong to the class of hybrid algorithms [37]. By their very nature, these algorithms cost both time and money as they make intense use of the quantum hardware, which motivates us to search for a more direct way of designing efficient schedules.

A detailed analysis of the classical dynamics of the simulated annealing for the MIS problem reveals that the graphs with many suboptimal solutions are likely to trap the algorithm in local minima, hence missing the global solution [19]. This observation leads to the definition of the hardness parameter $\mathbb{H} = D_{|\text{MIS}|-1}/(|\text{MIS}|D_{|\text{MIS}|})$, where D_k is the degeneracy of the independent sets of size k . On the basis of the theory of Markov chains, \mathbb{H} is shown to determine the performance of simulated annealing as it provides a lower bound on the inverse of its spectral gap and, by extension, on the hitting time for finding the solution. By analogy with the adiabatic theorem [6], this suggests that the hardness parameter may play a key role during the optimization of the schedules in the quantum setting, which is the starting point of our study.

In what follows, we show how a precomputation of optimized schedules for small graphs can lead to highly efficient protocols for graphs of larger size on the quantum device [38]. First, we review the MIS encoding in Rydberg atoms, emphasizing the importance of well-chosen boundary conditions. Then, in Sec. II we describe how to optimize the schedules on the basis of numerical simulations of small graphs. Finally, in Sec. III we present the results of cloud quantum computing demonstrations. Detailed information and calculations are provided in the appendices.

* Contact author: contact@gradiom.ch

A. MIS encoding in Rydberg atom arrays

The analog quantum dynamics of N atoms is governed by the Rydberg Hamiltonian $H = H_{\text{drive}} + H_{\text{cost}}$, where the driving part and the cost function are [19]

$$\frac{H_{\text{drive}}(t)}{\hbar} = \frac{\Omega(t)}{2} \sum_{i=1}^N e^{i\phi(t)} |0\rangle_i \langle 1| + \text{H.c.}, \quad (1a)$$

$$\frac{H_{\text{cost}}(t)}{\hbar} = -\Delta(t) \sum_{i=1}^N \hat{n}_i + \sum_{i < j} V_{ij} \hat{n}_i \hat{n}_j. \quad (1b)$$

In these equations, Ω is the Rabi drive amplitude, ϕ its phase, Δ the detuning, and $\hat{n}_i = |1\rangle_i \langle 1|$ detects the Rydberg excitation of the i th atom. The two-body potential is $V_{ij} = C_6/|\mathbf{r}_i - \mathbf{r}_j|^6$, with C_6 a constant for the van der Waals interaction between two Rydberg states at positions \mathbf{r}_i and \mathbf{r}_j . Because of the large decay exponent, this interaction prevents the presence of any doubly excited state if two atoms are close together but has a negligible impact if they are further apart. This enables the encoding of MIS problems on unit disk graphs, where the so-called blockade radius of the Rydberg interaction corresponds to the maximum distance between any two connected vertices of the graph, as illustrated in Refs. [16, 39]; see Appendix A for the mathematical description of this encoding.

The boundary conditions at initial and final times t_i and t_f of the adiabatic quantum computation are usually stated as follows:

$$\Omega_i = \Omega_f = 0, \quad (2a)$$

$$\Delta_i < 0 < \Delta_f. \quad (2b)$$

In practice, we implement the first inequality as $\Delta_i \leq -\delta_\Delta$, where δ_Δ is a small positive constant that incorporates the main sources of error in the quantum hardware, so that it is ensured that all atoms start in the easy-to-prepare ground state $|0\rangle$. Regarding the MIS encoding, the second inequality turns out to be necessary but not sufficient, as the final detuning has to lie in a narrow interval that depends on the graph geometry, see Appendix A 2. For instance, the lower and upper bounds of the detuning for unit disk graphs on a square lattice are given by

$$\Delta_{\text{LB}} = \frac{V_0}{12} \leq \Delta_f \leq \frac{V_0}{8} = \Delta_{\text{UB}}, \quad (3)$$

where $V_0 = C_6/a^6$ is the interaction strength between adjacent nodes separated by distance a . Note that such bounds are not universal, but they are satisfied by the vast majority of graphs for a given lattice.

B. Quantum hardware

Throughout this paper, we consider QuEra's Aquila device, whose characteristics are described in detail in

Ref. [25] and which is easily accessible through the AMAZON BRAKET interface [40]. Of course, all results extend to other devices and frameworks such as Pasqal's PULSER and also to other types of lattices (e.g., triangular) [41, 42]. The interaction coefficient C_6 between two excited states in Aquila is $5\,420\,503\,\text{MHz}\,\mu\text{m}^6$, and two limitations are particularly important in our study: first, the maximum duration of the protocol $t_{\text{max}} = 4\,\mu\text{s}$ to ensure a coherent evolution, and second, the maximum Rabi frequency $\Omega_{\text{max}} = 15.8\,\text{MHz}$ due to the limited laser power for driving the ground-Rydberg transition. We ignore the hardware errors in the simulations, but they could be taken into account to fine-tune the results. The only error that we consider here is the noise $\delta_\Delta \approx 1\,\text{MHz}$ in the global detuning since it plays a role in the upper bound of Δ_i . Unless otherwise specified, all units are micrometers, microseconds, and megahertz in what follows.

In Aquila, the Rabi amplitude and the detuning must be defined as piecewise linear and not smooth functions, while the phase must be piecewise constant. However, the step size can be as small as $0.05\,\mu\text{s}$, which results in 80 intervals for the longest coherent evolution. The schedules are therefore well approximated in the quantum hardware, but one could slightly improve the results of the demonstrations by taking into account this hardware capability in the numerical simulations.

II. NUMERICAL OPTIMIZATION

We consider a fixed set of 500 representative graphs of size 8 to 17, which allows us to perform fast numerical simulations and to use efficient deterministic optimization algorithms, see Appendix C. This dataset is such that the correlation between the size of the graphs and their hardness parameter is minimized. Therefore, the results that depend principally on \mathbb{H} can be extrapolated, to a certain extent, to graphs of any size.

In this work, we focus on the probability to reach a MIS solution at the end of the adiabatic evolution, which we denote by P_{MIS} and use as the score function to be optimized for some parametrization Θ of the schedules:

$$P_{\text{MIS}}(\Theta) = \sum_{i=1}^{D_{\text{MIS}}} \left| \langle \psi(\Theta, t_f) | \text{MIS}_i \rangle \right|^2, \quad (4)$$

where $|\psi(\Theta, t_f)\rangle$ is the final quantum state and $|\text{MIS}_i\rangle$ is the basis vector that corresponds to the i th solution of the MIS problem. Note that most studies consider the *approximation ratio* instead (normalized mean energy of the final state), but in our opinion only the lowest energy level and not the full energy spectrum has practical utility because of the very definition of the hardness parameter.

Following the “best practices” listed in Ref. [25], we consider protocols for which the Rabi amplitude $\Omega(t)$ reaches Ω_{max} during the evolution, so that the associated dynamic blockade radius R_b becomes $(C_6/\Omega_{\text{max}})^{1/6} \approx$

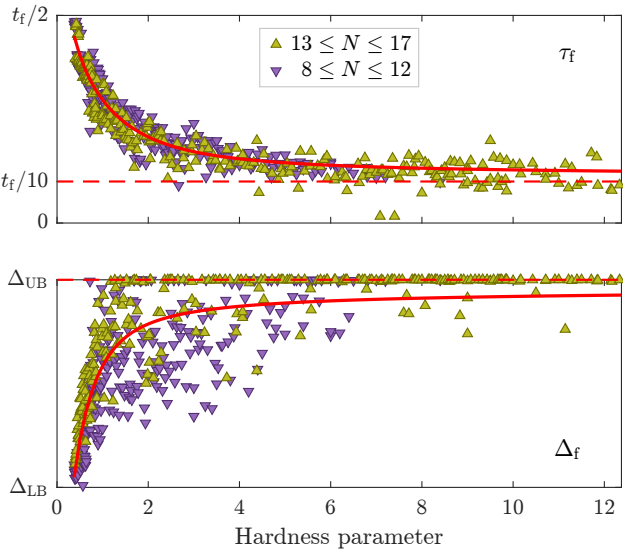


FIG. 1. Optimum parameters of the linear schedules for each graph of the dataset. These values depend on \mathbb{H} and converge to a constant (dashed red lines) for sufficiently hard graphs. This behavior is particularly strong for τ_f (top) and Δ_f (bottom) at the end of the adiabatic evolution, with no statistical difference between the smallest graphs (purple triangles) and the largest ones (yellow-green triangles). We fit all points to extract a smooth and monotonic dependence on \mathbb{H} (thick red lines).

8.4. In order to generate a unit disk graph on the nearest and next-nearest neighbors of a square lattice, this radius should satisfy $\sqrt{2}a < R_b < 2a$, and consequently $4.2 < a < 5.9$. We set $a = 5$, which is close to the geometric mean of these bounds and which yields good results in preliminary calculations. We consider a fixed evolution time $t_f = 1$ so that P_{MIS} varies as much as possible depending on the various protocols; much shorter or longer times lead to either extremely bad or extremely good results independently of the precise shape of the schedules.

In the following sections, we optimize and compare two paradigmatic protocols based on either piecewise linear or counterdiabatic schedules.

A. Piecewise linear protocol

The typical adiabatic protocol is based on piecewise linear schedules with two breakpoints, where Ω is slowly ramped up, then Δ is ramped from negative to positive, and finally Ω is ramped down; see Fig. 3.1b in Ref. [25] or Fig. 2c in Ref. [43]. Usually, these schedules are symmetric in the sense that the initial and final ramp times τ_i and τ_f are equal, and that the initial and final detunings Δ_i and Δ_f have opposite values. In our case, we are looking for schedules that are as general as possible, so we keep these parameters independent. Moreover, we

do not impose the condition that the breakpoints of Ω coincide with those of Δ .

After a few optimization steps, it appears that the flat portions of the detuning tend to vanish; we therefore consider a simple linear function for this schedule. Then we optimize the four remaining parameters ($\tau_i, \tau_f, \Delta_i, \Delta_f$) for each graph of the dataset. A noticeable observation is that the optimum parameters depend mostly on the hardness parameter and not on the size of the graph. Consequently, we can fit these data to generate a model of optimized schedules, as illustrated in Figs. 1 and 2.

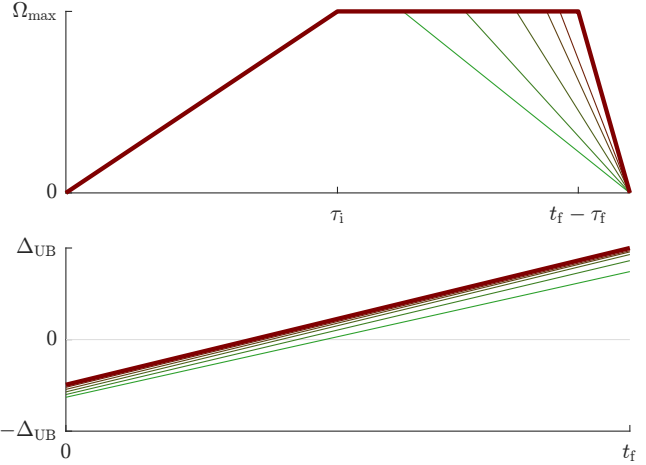


FIG. 2. Optimized piecewise linear schedules with four free variables. The Rabi amplitude (top) and the detuning (bottom) depend on the hardness of the graph and are illustrated here for $\mathcal{HP} \in \{0.5, 1, 2, 4, 8\}$ (thin lines, from green to maroon) and in the limit $\mathbb{H} \rightarrow \infty$ (thick dark maroon line). In this limit, the optimized values become $\tau_i \approx t_f/2$, $\tau_f \approx t_f/10$, $\Delta_i \approx -\Delta_{UB}/2$, and $\Delta_f = \Delta_{UB}$.

The hardness-dependent linear schedules yield very good results compared with existing protocols, which motivates us to go one step further by considering two more degrees of freedom (τ_m, Δ_m) for the detuning; see Fig. 3. The resulting optimized schedules are still easily implementable, yet they perform much better than all benchmark protocols; see Sec. II C.

Let us now provide some hints about the performance of the hardness-dependent linear schedules. The adiabatic condition for quantum computing is traditionally given by [6]

$$t_f \gg \max_{s \in [0,1]} \frac{|\langle \varepsilon_1(s) | \partial_s H(s) | \varepsilon_0(s) \rangle|}{|\varepsilon_1(s) - \varepsilon_0(s)|^2} = t_{\text{ad}}, \quad (5)$$

where $s = t/t_f$ is the dimensionless time, $|\varepsilon_0(s)\rangle$ is the instantaneous ground state of $H(s)$ with energy $\varepsilon_0(s)$, and $|\varepsilon_1(s)\rangle$ is any of the first excited states; for simplicity, we consider only the nondegenerate MIS instances here. In particular, Eq. (5) implies that the minimum energy gap $\Gamma = \min_s \varepsilon_1(s) - \varepsilon_0(s)$ should be large to maintain adiabaticity. Unsurprisingly, this gap gets smaller as the

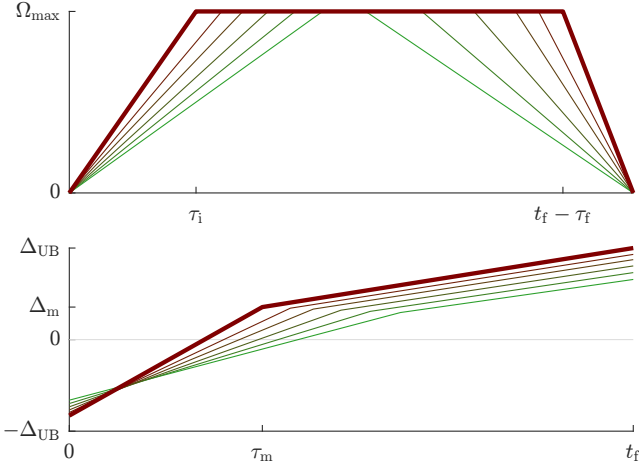


FIG. 3. Optimized piecewise linear schedules with six free variables. In this case, τ_i displays a clear dependence on \mathbb{H} . In the limit of infinite hardness, the optimized values are $\tau_i \approx 0.22t_f$ and $\tau_f \approx 0.12t_f$ for the Rabi amplitude (top) and $\Delta_i \approx -0.83\Delta_{UB}$, $\tau_m \approx 0.34t_f$, $\Delta_m \approx 0.36\Delta_{UB}$, and $\Delta_f = \Delta_{UB}$ for the detuning (bottom).

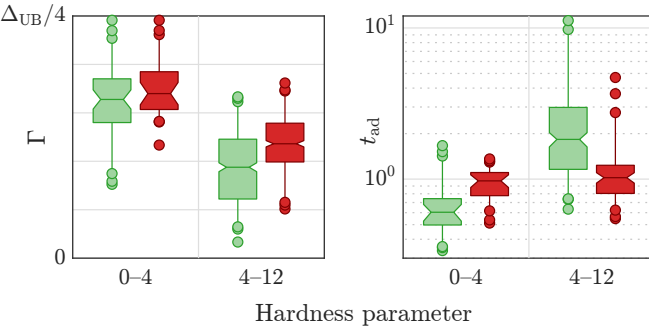


FIG. 4. Adiabatic criteria for the \mathbb{H} -linear protocol with six parameters. Left: Minimum energy gap for “easy” ($\mathbb{H} \leq 4$) and “hard” ($\mathbb{H} > 4$) graphs, based on the schedules illustrated in Fig. 3 with $\mathbb{H} = 1$ (light green) and $\mathbb{H} \rightarrow \infty$ (maroon). The gap by itself does not explain the hardness dependence of the optimum schedules, as shorter ramp times of the detuning (maroon boxes) are slightly beneficial for all graphs. Right: Corresponding adiabatic timescales. In this case, t_{ad} is indeed minimized if one applies the schedules according to the hardness of the graphs (leftmost and rightmost boxes).

hardness parameter increases: from the numerical simulations of the linear schedules with six parameters, we find $\Gamma \propto \exp(-\alpha\mathbb{H}^\beta)$ with $\alpha \approx 0.76$ and $\beta \approx 0.36$. In this respect, it seems counterintuitive that the Rabi amplitude should be ramped up and down more rapidly for harder graphs; see Fig. 3. Faster variations are likely to introduce stronger diabatic transitions which, in this case, would not be compensated by a larger gap to satisfy the adiabatic condition. However, we show in Fig. 4 that the optimized schedules do minimize the timescale t_{ad} on average, which confirms that adiabaticity lies at the heart of the protocol’s performance.

B. Counterdiabatic protocol

The limited coherence time of the quantum state in the hardware is a major source of error in adiabatic computing. Well-established methods to overcome such limitations include the shortcuts to adiabaticity, among which is the CD driving [44]. The idea of the CD driving is to add a gauge potential to the adiabatic Hamiltonian such that the transitions between eigenstates are suppressed during the evolution. However, the calculation of the exact gauge potential is very difficult in general, and these mathematical terms may not be always adapted to an implementation in the quantum hardware. Nevertheless, by ignoring the interactions of the Rydberg Hamiltonian, one is able to find a suitable gauge potential that utilizes the phase of the Rabi drive [32]. In this study, we propose to generalize the adiabatic schedules of this so-called analog counterdiabatic quantum computing (ACQC) protocol as follows:

$$\Omega_{ad}(t) = \Omega_{max} \sin\left(\frac{\pi}{2} \sin(\theta_{\Omega}(t))\right)^2, \quad (6a)$$

$$\Delta_{ad}(t) = \frac{\Delta_i + \Delta_f}{2} + \frac{\Delta_i - \Delta_f}{2} \cos(\theta_{\Delta}(t)), \quad (6b)$$

where $\theta(t)$ is any monotonic smooth function that ranges from 0 to π ; here we set $\theta_{\Omega,\Delta}(t) = \pi t/t_f$. Moreover, on the basis of the variational procedure described in Ref. [31], we improve on the ACQC protocol by including the Rydberg interactions in the calculation of the CD terms, thus adapting the gauge potential to each different graph; see Appendix B. The detuning is not altered by this operation, whereas the Rabi drive becomes

$$\Omega = \sqrt{\Omega_{ad}^2 + \Omega_{cd}^2}, \quad (7a)$$

$$\phi = \arctan(\Omega_{cd}/\Omega_{ad}), \quad (7b)$$

with

$$\Omega_{cd} = \frac{\Omega_{ad}\dot{\Delta}_{ad} - \dot{\Omega}_{ad}\Delta_{ad} + \dot{\Omega}_{ad}T_1\nu}{\Omega_{ad}^2 + \Delta_{ad}^2 - 2\Delta_{ad}T_1\nu + T_2\nu^2} \quad (8)$$

and where $0 \leq \nu \leq V_0$ is an additional free parameter that interpolates between the standard gauge potential and the generalized gauge potential; see Appendix B 2 b. In the latter equation, the variables T_1 and T_2 depend on the interaction terms V_{ij} and are therefore specific to the graph to be solved. As expected, the CD contribution vanishes for $t_f \rightarrow \infty$ since both $\dot{\Omega}_{ad}$ and $\dot{\Delta}_{ad}$ tend to zero in this limit.

Similarly as for the piecewise linear protocol, we optimize the schedule parameters $(\Delta_i, \Delta_f, \nu)$ for all graphs of the dataset; see Fig. 5. The interpolating coefficient ν tends to a strictly positive value for the hardest graphs, indicating that the generalized gauge potential plays an important role in the CD protocol. Note that the easy graphs exhibit optimized values of Δ_f that are smaller than the statistically determined constant Δ_{LB} . This

is because the exact lower bounds on the detuning are much smaller in that case; see Fig. 12 in Appendix A 2. The shape of the CD phase is highly nontrivial, and we observe a strong shift toward higher values of the detuning for hard MIS instances; see Fig. 6. Finally, we also tried to further improve the results by considering more evolved θ functions—in particular, to mimic the skewed shape of the Rabi amplitude in Fig. 2—but no significant gain was found in this case.

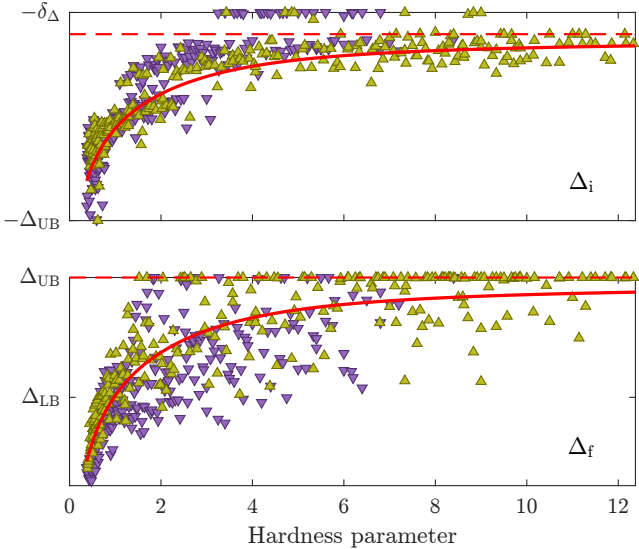


FIG. 5. Optimum parameters for the CD schedules. The initial detuning (top) reaches the upper bound $-\delta_\Delta$ for several graphs but tends to a lower value $\Delta_i \approx -\Delta_{UB}/10$ for the hardest graphs. The final detuning (bottom) also increases with the hardness parameter and quickly reaches the limit Δ_{UB} . The coefficient ν (not shown) displays a similar behavior and tends to approximately $V_0/80$ in the current setting.

C. Results

In Fig. 7, we compare the probability P_{MIS} to reach the solution for four protocols: the piecewise linear and ACQC protocols defined in Ref. [32], which serve as benchmarks, and their generalized and hardness-dependent counterparts described in the previous sections. Note that $a = 5.5$ for the benchmark protocols but $a = 5$ in our study. The \mathbb{H} -linear protocol (with six degrees of freedom) yields the best results for all graphs, and in particular for the hard ones with a tenfold improvement over the benchmark.

Graph-to-graph comparisons are illustrated in Fig. 8. As for the optimized schedule parameters, we observe that the values of P_{MIS} depend mostly on the hardness parameter and not on the size of the graphs. For instance, the success probabilities for the \mathbb{H} -linear protocol range from 0.59 ($\mathbb{H} = 4.20$) to 0.99 ($\mathbb{H} = 0.46$) for $N = 10$, and

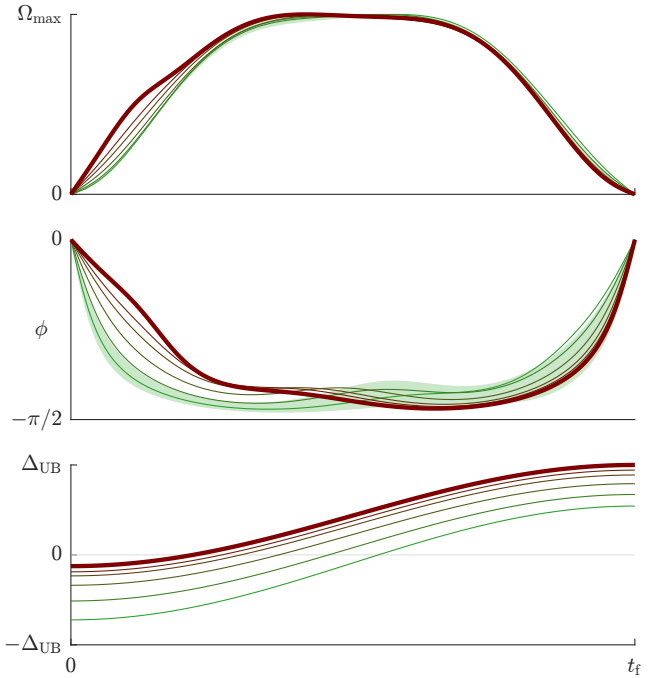


FIG. 6. Optimized counterdiabatic schedules with three free variables. Unlike the detuning (bottom), the Rabi amplitude (top) and phase (middle) depend not only on \mathbb{H} but also on t_f and on the graph-dependent variables T_1 and T_2 . Here the curves are displayed for $t_f = 1$ and for the mean values of the dataset $\bar{T}_1 \approx 0.93$ and $\bar{T}_2 \approx 1.46$. The light-green area represents the variation solely due to T_1 and T_2 for $\mathbb{H} = 0.5$.

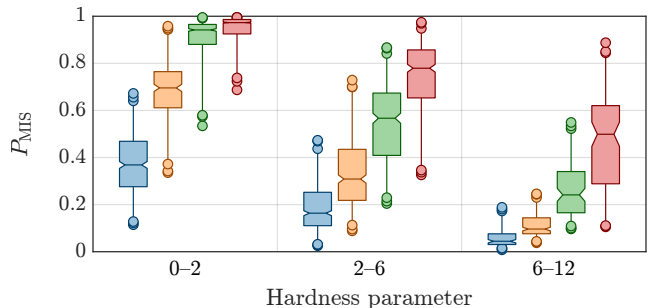


FIG. 7. Box plot of the probability of reaching the MIS depending on the hardness of the 500 graphs of the dataset. The piecewise linear (blue) and ACQC (orange) protocols serve as benchmarks. For hard graphs, the generalized \mathbb{H} -ACQC (green) and \mathbb{H} -linear (red) protocols developed in this study lead to an average success probability that is increased by approximately 150% and 1000%, respectively.

from 0.11 ($\mathbb{H} = 9.71$) to 0.98 ($\mathbb{H} = 0.52$) for $N = 17$.

III. CLOUD QUANTUM COMPUTING DEMONSTRATIONS

On the basis of thorough numerical simulations, we showed in the previous section that hardness-dependent

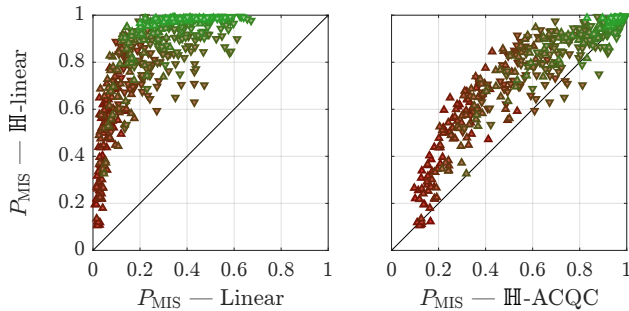


FIG. 8. Graph-to-graph comparisons of P_{MIS} . Left: The \mathbb{H} -linear protocol developed in this study leads to a 3.6-fold mean improvement on the linear protocol described in Ref. [32]. Right: Except for rare instances, the hardness-dependent piecewise linear protocol always beats its ACQC counterpart. Note that P_{MIS} depends strongly on \mathbb{H} but not on N (upward or downward triangles), with low success probabilities for the hard graphs (maroon) and nearly perfect results for the easy ones (green).

schedules lead to high probabilities of reaching the MIS solution. We first extend these results to the hardware and to graphs that are not part of the dataset used in the optimization. First, we consider a small set of “toy graphs” that we can still simulate classically to ensure that the various protocols are correctly run in Aquila. Then we apply the models to large graphs made up of 137 vertices to verify that the hardness parameter and not the size of the graph is indeed the most relevant property when solving the MIS problem.

For all examples, we use 720 shots (repetitions of the adiabatic evolution) to get enough data for a statistical comparison of the methods. We choose this specific value because it is a multiple of 9, 12, and 16, which are the maximum number of copies of the small graphs (3×3 and 3×4 lattices with $a = 5$ and $a = 5.5$) that fit and can be run simultaneously in the hardware. We consider only the shots in which the lattice is correctly filled by atoms. The typical probability of failing to occupy a site in Aquila is 0.007 (see Sec. 1.5 in Ref. [25]), and in practice we get 684 ± 7 and 380 ± 14 valid shots for the small and the large graphs, respectively.

A. Toy graphs

In Fig. 9, we display the probability of reaching the MIS solution for the 11 toy graphs defined in [33]. As in that article, we set $t_f = 0.7$ so that the probabilities of success are distributed around 50%. We observe good agreement between numerical simulations and the corresponding results obtained on hardware, especially for the benchmark protocols. A possible reason for the optimized schedules yielding outcomes that are slightly lower than expected may be the choice of a smaller lattice spacing or the larger gradient of Ω at the end of the evolution; many other sources of error could explain these differ-

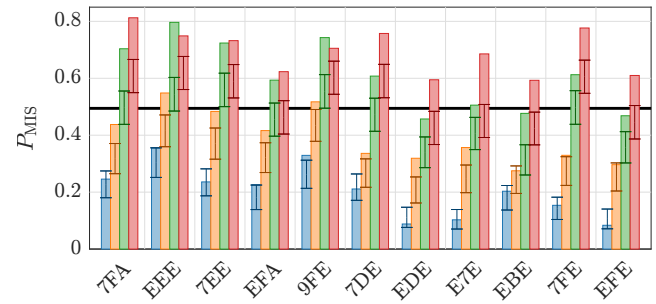


FIG. 9. Probability of reaching the MIS solution for the 11 toy graphs. The rectangular bars are numerical results and the error bars are the results of the demonstration (95% confidence intervals). The ranking of the four protocols studied is the same as in Fig. 7, with $\mathbb{H} \in [2, 3]$ here. The horizontal black line represents the average success probability obtained by the Bayesian optimization in Ref. Finzgar2024 (see Fig. 9 therein), which performs better than the benchmarks (blue and orange) but not as well as the hardness-dependent protocols (green and red).

ences—see Sec. 1.5 in [25] for an exhaustive list. Nevertheless, the \mathbb{H} -linear protocol still performs better on the hardware than the linear and CD benchmarks, with a threefold mean improvement and a twofold mean improvement, respectively.

B. Large graphs

We now turn to large graphs, which are of much greater interest in real applications. We consider three of the four graphs studied in Ref. [33] (see Fig. 10 therein), which consist of 137 vertices and whose hardness parameters extend over 3 orders of magnitude ($\mathbb{H} \approx 14, 126$, and 1435). In addition, we generate one very easy graph of the same size to span yet another order of magnitude ($\mathbb{H} \approx 1.4$); see Fig. 10. In these examples, the hardness parameter can still be computed by an advanced classical algorithm; namely, by the `GenericTensorNetworks` `Julia` library [45, 46]. However, in general, this parameter cannot be considered to be known beforehand as it depends on the MIS solution, which is the very target of the demonstrations. Therefore, we apply the optimized schedules in the limit $\mathbb{H} \rightarrow \infty$ in what follows, and we focus on the piecewise linear protocols as they are expected to yield the best results.

Contrarily to the small graphs, we now use the full coherent time of the hardware, i.e. $t_f = t_{\text{max}} = 4$. We want the probability of finding a MIS solution to be as high as possible for the hardest instances. Moreover, we post-process all data of the demonstrations such that the measured outcomes become valid maximal independent sets. To this end, we use the greedy procedure described in Sec. S2.3 in Ref. [19]: First, we remove any of two neighboring vertices until the sets become independent. Second, we include a vertex at any free site with no neighbor un-

til the sets are maximal. The same procedure applied to an empty configuration is used as a classical benchmark, which highlights the relative gain obtained with the quantum protocols [25, 36].

The results are summarized in Fig. 10: The MIS solution is never found by the classical greedy algorithm and is obtained by the standard linear protocol only for the easiest graph. In contrast, the \mathbb{H} -linear protocol leads to the solution for all but the hardest graph, which indicates a clear improvement over the existing protocols.

IV. DISCUSSION AND OUTLOOK

In this work, we have shown how to design the adiabatic schedules of the Rydberg Hamiltonian to efficiently solve the MIS problem on unit disk graphs.

First, a statistical investigation of the conditions for which the final quantum state encodes the MIS solution has revealed that the final detuning should lie in a narrow interval. To our knowledge, these are the tightest bounds ever mentioned. We believe that choosing a final detuning in that interval would improve the results of many other studies, either in terms of success probability or in terms of the number of optimization steps. Indeed, the application of adiabatic protocols in which the final ground state does not correspond to the sought solution can only lead to poorly performing algorithms.

Second, the individual optimization of numerous small graphs has shown that the optimum parameters of the schedules depend mostly on the hardness parameter and only marginally on the size of the graph. Through extensive classical simulations of small systems, we have generated adiabatic schedules that perform extremely well also when applied to much larger graphs; only the hardest instances are not solved by our protocol. Obviously, improvements in the hardware would greatly help in this regard, especially if they lead to a longer coherent evolution time. Since quantum technology is evolving rapidly, this could be the case soon. However, because of the combinatorial nature of the hardness parameter, very hard MIS problems exist only in sufficiently large graphs, so our numerical study should be extended to larger graphs to address this issue. We believe that improved schedules could be easily found by consideration of slightly larger systems, with up to about 25 vertices, or even larger ones

with the use of tensor network techniques for the simulations whenever appropriate [47].

We have focused our work on two families of schedules; namely, piecewise linear and smooth counterdiabatic functions. The phase of the Rabi drive is non-constant only in the latter case, and we have developed a generalized version of the ACQC protocol [32] to make it specific to each graph. However, when correctly parametrized, the somehow simpler \mathbb{H} -linear protocol performs better in almost all numerical simulations. This difference is even more pronounced in demonstrations, as the smooth CD schedules have to be converted into piecewise linear or constant functions. We have used a maximum number of six free parameters in the optimization, but more general functions may be investigated since the method described in this work applies to any kind of schedule. Moreover, it would be interesting to develop models of optimized schedules that do not depend only on the hardness parameter but that depend also on other global properties of the graphs, e.g., the mean degree or the mean eccentricity of the vertices. On the basis of machine learning, such additional predictors could improve the fitting of the schedule parameters.

We think that hybrid classical-quantum algorithms could take advantage of our protocols and, more generally, of precomputed optimized schedules: instead of searching in the huge space of all parameters, one could consider lower-dimensional meaningful ansatzes, such as the \mathbb{H} parametrization of the schedules or the principal component of the residuals of the fitted parameters.

Finally, we believe that the piecewise linear protocols developed in this study should serve as a benchmark for any future adiabatic algorithm that aims to solve the MIS problem with Rydberg atoms. In particular, the most basic version of this protocol with only four free parameters and in the limit of infinite hardness admits a very simple mathematical description—see Fig. 2—and it leads to relatively good results regardless of the specific graph to be solved.

DATA AVAILABILITY

The data that support the findings of this article are openly available [48].

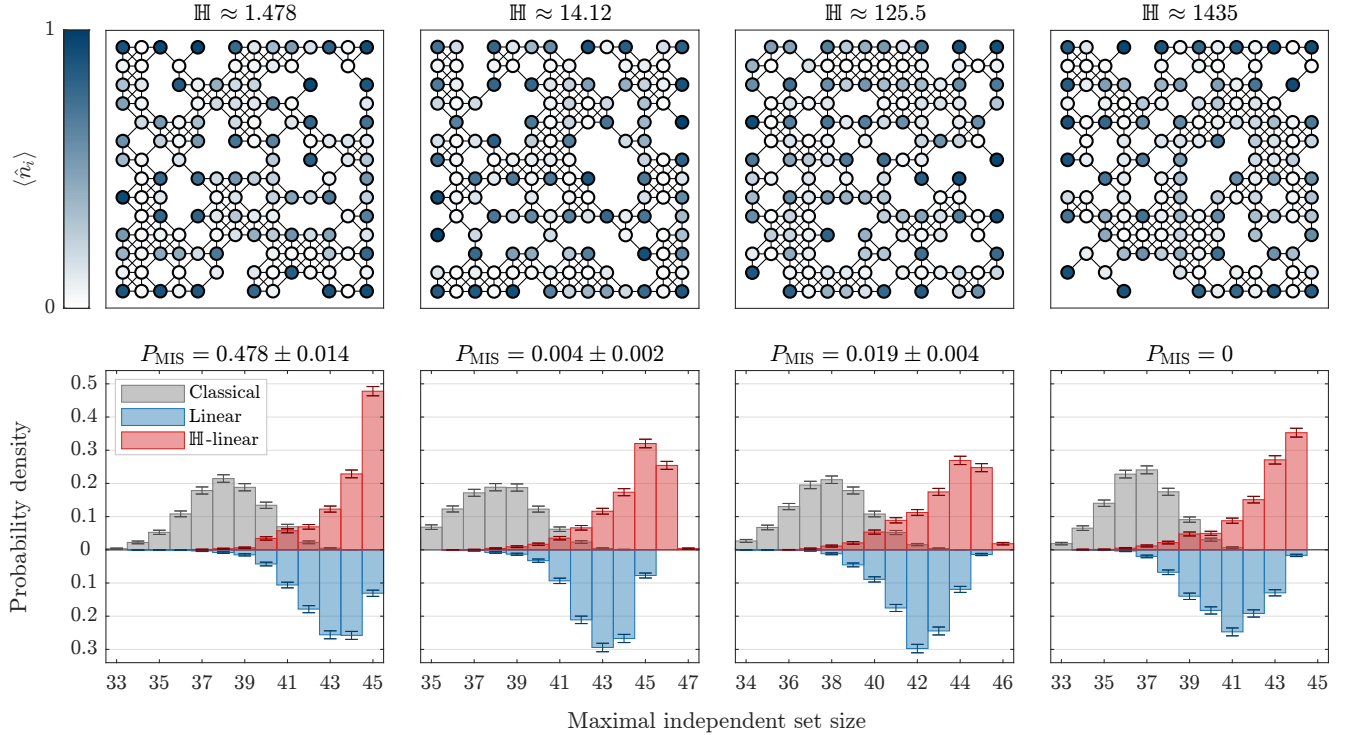


FIG. 10. Demonstrations for large unit disk graphs. Top: Four graphs with 137 vertices each and whose hardness parameters span 4 orders of magnitude; the three hardest graphs are taken from [33]. In shades of blue, the probability $\langle \hat{n}_i \rangle$ to measure the i th atom in the Rydberg state $|1\rangle$ at the end of the \mathbb{H} -linear protocol. Because of the high degeneracy of the MIS, some vertices are equally measured in the ground state or the excited state. Bottom: Results of the demonstrations (after a minimal postprocessing) to find an independent set of a given size, with the MIS solution at the rightmost bin. The error bars represent the 95% confidence intervals. The classical greedy algorithm (gray) fails to find the solution in all cases. The benchmark linear protocol (blue) reaches the MIS in the easiest case but fails for any harder instance. Finally, the \mathbb{H} -linear protocol is able to find the MIS except for the hardest graph; the corresponding values of P_{MIS} are indicated. The success probabilities for the two CD protocols (not shown) lie between those of the two linear protocols.

APPENDIX A: GROUND STATE ENCODING OF THE MAXIMUM INDEPENDENT SET PROBLEM

Given a simple undirected graph $\mathcal{G} = (V, E)$ with vertex set V and edge set E , a subset $S \subseteq V$ is called independent if no pair of vertices in S are connected by an edge in E . In the MIS problem, we want to find the independent set of largest cardinality. If we denote by $x_i \in \{0, 1\}$ the absence or the presence of the vertex $i = 1, \dots, N$ in S , it is proven that the MIS solution minimizes the cost function [49, 50]

$$\mathcal{C}(x_1, \dots, x_N) = - \sum_{i \in V} \Delta x_i + \sum_{ij \in E} V_{ij} x_i x_j \quad (\text{A1})$$

if $0 < \Delta < V_{ij}$ for all $ij \in E$. In analog quantum computing with arrays of Rydberg atoms, \mathcal{G} is a unit disk graph that connects the nearest and next-nearest neighbors of a square lattice. If we ignore the interactions between farther atoms, for a non-planar graph (i.e., when crossing diagonals belong to it), the MIS condition becomes

$$0 < \Delta_f < \frac{C_6}{(\sqrt{2}a)^6} = \frac{V_0}{8}, \quad (\text{A2})$$

where a is the lattice spacing, $V_0 = C_6/a^6$ is the interaction strength between adjacent atoms, and $\Delta_f = \Delta(t_f)$ is the detuning at the final evolution time t_f . In several investigations, it is implicitly assumed that the inequalities (A2) hold for all unit disk graphs due to the sharp Rydberg blockade transition. However, in what follows we show that the condition $0 < \Delta_f$ is necessary but not sufficient.

1. Nonexistence of a lower bound on the detuning

The van der Waals interaction decays quickly with the distance between atoms, but it cannot be ignored for distances close to the blockade radius. As an example, consider the graph that consists of three atoms in a row with distance $2a$ between its extremities; see Fig. 11(a). In this case, the MIS solution is $(1, 0, 1)$, which corresponds to an energy of $-2\Delta_f + V_0/64$. By listing the energy of all other configurations, we find the following conditions on Δ_f such that $|101\rangle$ is indeed the ground state of the final Rydberg Hamiltonian:

$$V_0/64 < \Delta_f < 2V_0. \quad (\text{A3})$$

The upper bound is, of course, already satisfied in Eq. (A2) as it is a sufficient condition, but the value $V_0/64$ should be considered as a strict lower bound for any protocol; note that this bound is mentioned in Ref. [25]. The question is then to determine if there exists, for unit disk graphs in a square lattice, a finite lower bound on the detuning to ensure the equivalence between the classical MIS solution and the ground state of the quantum Hamiltonian. Unfortunately, the answer is negative. Consider the unit disk graph in Fig. 11(b), and the following two sets of vertices: S_0 , the MIS solution with $m + 1$ vertices on the main line (filled circles); S_1 , the m vertices located at the tip of the alternating upward and downward triangles (orange circles). If we take into account all pairwise interactions, the corresponding energies read

$$E_0 = -(m + 1)\Delta_f + \frac{V_0}{64} \sum_{i=1}^m \frac{m + 1 - i}{i^6}, \quad (\text{A4a})$$

$$E_1 = -m\Delta_f + \frac{V_0}{64} \sum_{i=1}^{\lfloor m/2 \rfloor} \left(\frac{m + 1 - 2i}{(4i^2 - 4i + 2)^3} + \frac{m - 2i}{(2i)^6} \right). \quad (\text{A4b})$$

For the ground state of the Hamiltonian to yield the MIS solution we must have $E_0 < E_1$, i.e., the detuning has to satisfy the inequality

$$\frac{V_0}{64} (\Sigma_0 - \Sigma_1) < \Delta_f, \quad (\text{A5})$$

where Σ_0 and Σ_1 stand for the sums on the right-hand sides of Eqs. (A4a) and (A4b). However, one can check that the difference $\Sigma_0 - \Sigma_1$ is always positive and becomes arbitrarily large for increasing m . In particular, this difference is larger than 8 for $m \geq 9$, leading to a contradiction with Eq. (A2).

In conclusion, there does not exist a value of the final detuning such that it is ensured that the Rydberg Hamiltonian encodes the MIS solution of all unit disk graphs.

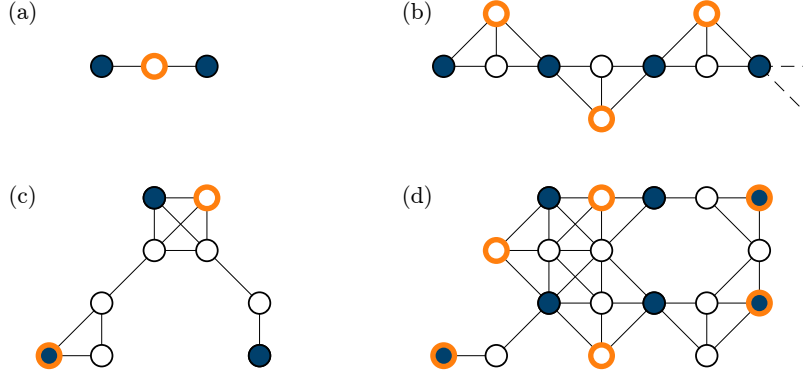


FIG. 11. Examples of unit disk graphs to study the lower bound on the final detuning. The MIS solution (filled circles) has a lower energy than the suboptimal configuration (orange circles) if and only if $\Delta_f > \Delta_{LB}$. (a) Reference graph used in Eq. (A3). (b) Graph with $N = 3m + 1$ vertices forming m alternating upward and downward triangles. For any $\Delta_f > 0$, there exists a value of m such that the suboptimal configuration is energetically favorable. (c), (d) Two non-planar graphs with very different lower bounds: (c) $\Delta_{LB} \approx V_0/1017$ ($\mathbb{H} \approx 0.42$) and (d) $\Delta_{LB} \approx V_0/11.49$ ($\mathbb{H} = 15$).

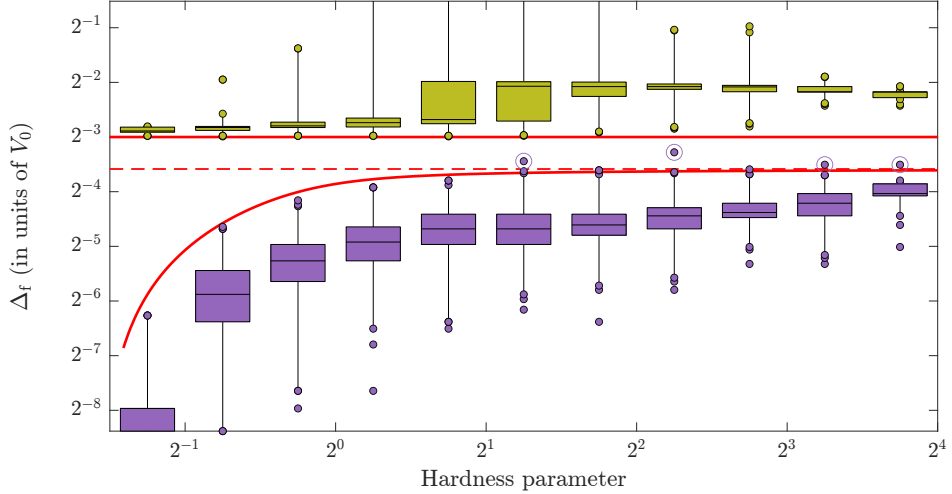


FIG. 12. Box plot of the lower bounds Δ_{LB} (purple) and upper bounds Δ_{UB} (yellow-green) on the detuning Δ_f such that the ground state of the Hamiltonian encodes the MIS solution. Calculations are performed on 10 000 nonisomorphic unit disk graphs with 8–19 vertices. All but four graphs satisfy $\Delta_{LB} \leq V_0/12$ (dashed red line) while Δ_{UB} is always strictly larger than $V_0/8$. It is interesting to note that, on average, easy graphs exhibit much smaller lower bounds than hard graphs (red curve); see also Fig. 11(c-d). Since the average value of Δ_{LB} quickly saturates for not-too-easy graphs, we are confident that these bounds can be effectively applied to graphs of any size.

2. Statistical analysis of the bounds on the detuning

As shown above, the final detuning has to be arbitrarily high if one wants to encode the MIS solution of any graph in the Rydberg Hamiltonian. However, this is not the case in general, as most graphs obey well-defined conditions on Δ_f . From an extensive analysis of 10 000 graphs—see Fig. 12—we find that more than 99.9% of all graphs satisfy the following bounds:

$$\Delta_f \in [\Delta_{LB}, \Delta_{UB}] = \left[\frac{V_0}{12}, \frac{V_0}{8} \right]. \quad (A6)$$

Interestingly, this interval is very close to the best range of parameters found by a variational optimization (see Fig. 6.1 in Ref. [25]) with $\Delta_{LB} = 28.91$ MHz and $\Delta_{UB} = 43.36$ MHz for QuEra’s Aquila device and $a = 5$ μm . Note that a statistical analysis is also performed in Ref. [19] (see Sec. S2 therein), where it is stated that about 99% of the MIS problems can be encoded in the ground state of a Rydberg Hamiltonian for well-chosen fixed parameters of

the quantum hardware. We strongly recommend considering the interval in Eq. (A6) when one is setting the final detuning of any adiabatic protocol for the MIS problem. A value that lies far outside this interval will likely lead to poor results simply because the ground state of the Hamiltonian does not correspond to the MIS solution.

APPENDIX B: GRAPH-DEPENDENT COUNTERDIABATIC DRIVING

For convenience, we set $\hbar = 1$ and $\phi(t) = 0$ in what follows, but all results can be extended to the general scenario. In this case, the Rydberg Hamiltonian reads

$$H(t) = \frac{\Omega(t)}{2} \sum_i \hat{X}_i - \Delta(t) \sum_i \hat{n}_i + \sum_{i < j} V_{ij} \hat{n}_i \hat{n}_j \equiv \frac{\Omega(t)}{2} \hat{X} - \Delta(t) \hat{n} + \hat{V}, \quad (\text{B1})$$

where $\hat{n}_i = |1\rangle_i \langle 1|$ and \hat{X}_i is the Pauli matrix $|0\rangle_i \langle 1| + |1\rangle_i \langle 0|$ acting on atom $i = 1, \dots, N$.

1. Approximate adiabatic gauge potential

The idea of the CD driving is to add a gauge potential \mathcal{A} to the Hamiltonian H such that the transitions between eigenstates are suppressed during a shortened adiabatic evolution:

$$\tilde{H}(t) = H(t) + \mathcal{A}(t), \quad (\text{B2})$$

where \mathcal{A} satisfies the equation [see Eq. (2) in Ref. [31]]:

$$[i\partial_t H - [\mathcal{A}, H], H] = 0. \quad (\text{B3})$$

If the interactions \hat{V} are ignored, it is shown in Ref. [32] that a solution of this equation exists:

$$\mathcal{A}_{V \rightarrow 0} = -\frac{1}{2} \frac{\Omega \dot{\Delta} - \dot{\Omega} \Delta}{\Omega^2 + \Delta^2} \hat{Y}. \quad (\text{B4})$$

This gauge potential leads to improved results compared with a simple adiabatic protocol, but one might expect even better results with a gauge potential that explicitly depends on the coefficients V_{ij} , hence being specific to the graph to be solved. To find such a generalized gauge potential, we consider the variational procedure that consists in minimizing the action [see Eq. (8) in Ref. [31]]

$$\mathcal{S}(\mathcal{A}_\lambda) = \text{Tr} (G^2(\mathcal{A}_\lambda)), \text{ with } G(\mathcal{A}_\lambda) = \partial_t H + i[\mathcal{A}_\lambda, H]. \quad (\text{B5})$$

Here we use the ansatz $\mathcal{A}_\lambda = -\hat{Y}\lambda(t)/2$ since the one-body Pauli matrices \hat{Y}_i are the only operators that contribute to the action while being implementable in the quantum hardware through the phase ϕ of the Rabi drive. One can easily check that \mathcal{S} is quadratic in λ and that the optimum value of this parameter is given by

$$\lambda = 2 \frac{\text{Tr} (\partial_t H [i\hat{Y}, H])}{\text{Tr} ([i\hat{Y}, H]^2)}. \quad (\text{B6})$$

On the basis of the algebraic properties of the Pauli matrices and the trace operator, this expression can be developed and simplified as follows:

$$\lambda = \frac{\Omega \dot{\Delta} - \dot{\Omega} \Delta + \dot{\Omega} T_1}{\Omega^2 + \Delta^2 - 2\Delta T_1 + T_2}, \quad (\text{B7})$$

where the normalized traces T_1 and T_2 are given by

$$N T_1 = 2^{-N} \text{Tr} (\hat{X} [i\hat{Y}, \hat{V}]) = \sum_{i < j} V_{ij}, \quad (\text{B8a})$$

$$N T_2 = 2^{-N} \text{Tr} ([i\hat{Y}, \hat{V}]^2) = \frac{1}{2} \sum_{i \leq j} \sum_{k \neq i, j} V_{ik} V_{kj}. \quad (\text{B8b})$$

As expected, the graph-dependent gauge potential \mathcal{A}_λ is equal to $\mathcal{A}_{V \rightarrow 0}$ in the case of vanishing interactions, with $T_1 = T_2 = 0$ in this limit. Because of the fast-decaying interaction between distant atoms, T_1 and T_2 do not scale with N as they represent average values of (nearly) local functions. For instance, T_1 is exactly half the mean degree of the underlying graph if one considers its adjacency matrix instead of the interaction terms in Eq. (B8a).

Finally, the driving amplitude and phase of the full Rydberg Hamiltonian \tilde{H} become

$$\tilde{\Omega} = \sqrt{\Omega^2 + \lambda^2}, \quad (B9a)$$

$$\tilde{\phi} = \arctan(\lambda/\Omega). \quad (B9b)$$

Note that λ and therefore $\dot{\Omega}$ should be equal to zero at the beginning and at the end of the protocol to satisfy the boundary conditions $\tilde{\Omega}(t_i) = \tilde{\Omega}(t_f) = 0$.

2. Practical application of the counterdiabatic driving

a. Hardware implementation

It follows from Eq. (B9a) that $\tilde{\Omega}$ is always larger than Ω , so it may exceed the maximum Rabi frequency Ω_{\max} of the quantum computer. In this case, we rescale the adiabatic function Ω by a factor $0 < \kappa < 1$ to satisfy the hardware constraint at any time t of the evolution:

$$\max_t \left\{ \tilde{\Omega}(\kappa \Omega(t), \Delta, T_1, T_2) \right\} = \Omega_{\max}.$$

Note that this is slightly different from rescaling $\tilde{\Omega}$ directly, as the relations (B7), (B9a), and (B9b) would not hold in that case.

b. Variational parameter

Since Eq. (B7) is a generalization of the counterdiabatic term proposed in Ref. [32] through the addition of T_1 and T_2 , it is interesting in an optimization context to consider a continuous interpolation between these two protocols. One possibility is to consider the interaction strength V_0 as a free parameter in the range $[0, C_6/a^6]$ when one is calculating the CD driving. To avoid any confusion with the fixed interactions in the Rydberg Hamiltonian, we denote by ν this free parameter. Numerically, this is equivalent to replacing T_1 and T_2 in Eq. (B7) by the following expressions:

$$T_1 = \nu T_1^{(0)}, \quad (B10a)$$

$$T_2 = \nu^2 T_2^{(0)}, \quad (B10b)$$

where $T_1^{(0)}$ and $T_2^{(0)}$ are the traces evaluated at $V_0 = 1$ in Eqs. (B8a) and (B8b). Another possibility would be to consider the two-variable parametrization $T_i = \nu_i T_i^{(0)}$, with $\nu_i \in [0, V_0^i]$ and $i \in \{1, 2\}$.

APPENDIX C: GRAPH DATASETS AND NUMERICAL IMPLEMENTATION

In the following sections, we first describe two sets of unit disk graphs $\mathcal{G} = (V, E)$ that are used in this study; the data are available on GitHub [48]. In all examples, we consider an underlying square lattice where the distance a between nearest-neighbors is 1 and where any pair of vertices in V is connected by an edge in E if the corresponding distance is smaller than or equal to $\sqrt{2}$. Then we detail the numerical method that is used to simulate the evolution of the quantum state under the action of the Rydberg Hamiltonian.

1. Graph datasets

Small graphs From 10 000 nonisomorphic graphs randomly generated, we choose 500 graphs such that the correlation between their hardness parameter and their order is as small as possible; see Fig. 13. More precisely, we apply the following rules to determine which graphs belong to the dataset:

- There are exactly 50 graphs for each order from 8 to 17.
- The hardness parameters are distributed as evenly as possible on a logarithmic scale from 0.375 to 12; in particular, no two graphs share the same hardness parameter, and exactly 100 graphs are contained in each bin $[3 \times 2^{i-4}, 3 \times 2^{i-3})$ with $i = 1, \dots, 5$.
- The distribution of the graph orders is as uniform as possible within each such bin.

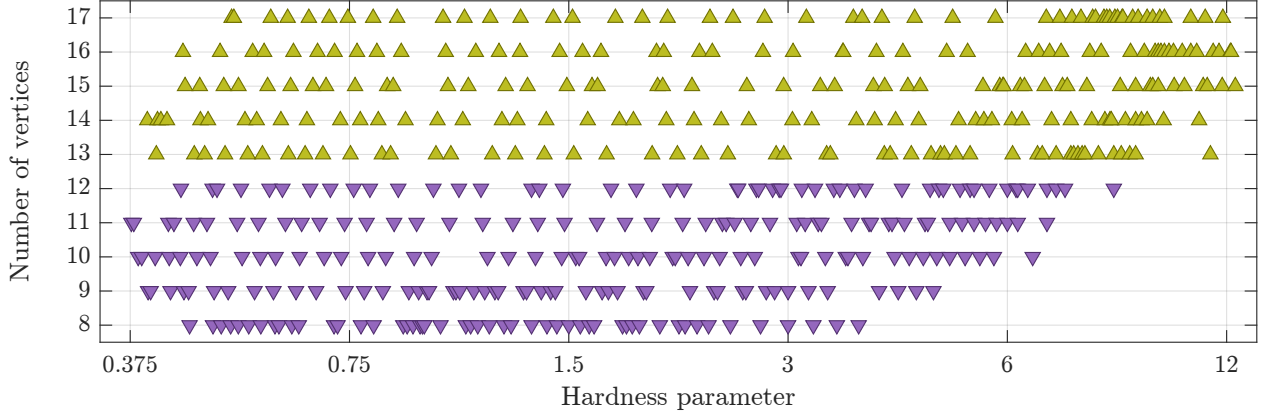


FIG. 13. Visualization of the hardness parameters \mathbb{H} and the orders of the 500 small graphs. Because of the combinatorial definition of the hardness parameter, graphs with few vertices (6–12 purple triangles) cannot generate very hard MIS instances. This explains why larger graphs (13–17 vertices, yellow-green triangles) are overrepresented in the range $\mathbb{H} \in [6, 12]$.

Toy graphs For completeness, we display in Fig. 14 the 11 toy graphs defined in Appendix C in [33]:

- The underlying square lattice has 4×3 sites.
- The order of the graphs is 9 or 10.
- There is only one MIS solution for each graph.

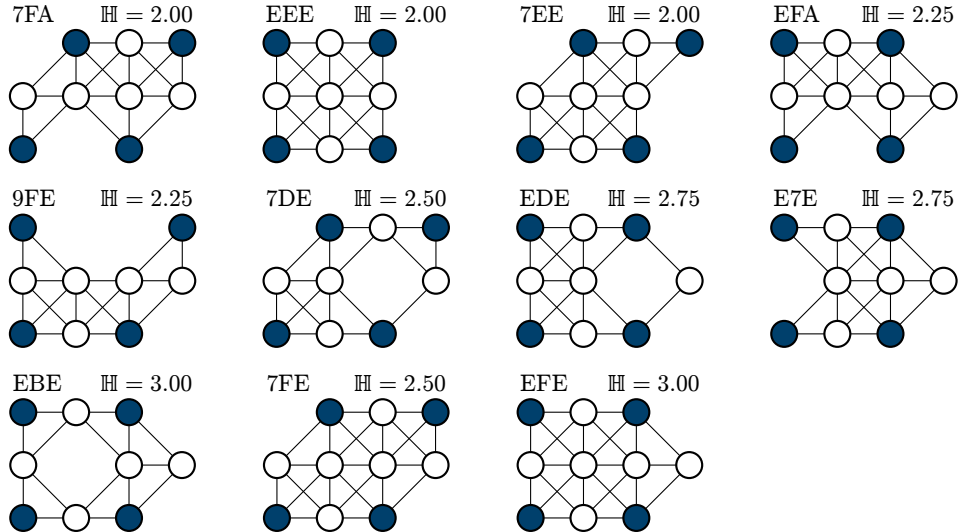


FIG. 14. The 11 toy graphs sorted by the number of vertices (nine or ten) and by hardness parameter (between 2 and 3). The unique MIS is highlighted with dark-blue circles. To refer to a specific graph, we generate the three-nibble identifiers as follows: the i th nibble (4-bit aggregation) is the hexadecimal symbol that represents the absence or presence of a vertex in the four sites of the i th row (from top to bottom).

2. Numerical implementation

Several software development kits exist to simulate the Rydberg evolution: for example, **BLOQADE** [51] and **AMAZON BRAKET** [40] for QuEra’s hardware, or **PULSER** [41] based on QuTiP for Pasqal’s technology. Nevertheless, we developed our own routines to get full control over all parameters and, more importantly, to fit exactly our needs. Optimization of hundreds of graphs for several protocols requires intense (classical) computing power, so we have to find the perfect balance between accuracy and speed. For example, for each graph of the datasets we precompute all time- and protocol-independent terms in the Hamiltonian, namely, the \hat{X} , \hat{Y} , \hat{n} , and \hat{V} operators; see Eq. (B1). We also use an explicit Runge-Kutta method of order 2 [52] to integrate the time-dependent Schrödinger equation, which turns out to be sufficiently accurate and much faster than the default order 8 method (**DOP853** in **PYTHON** or **VERN8** in **JULIA**). The initial state of this ordinary differential equation is $|0\rangle^{\otimes N}$, which corresponds to the unique ground state of the Rydberg Hamiltonian with $\Omega = 0$ and $\Delta < 0$.

a. Blockade subspace

Besides the above-mentioned implementation aspects, a crucial ingredient is the correct use of the blockade subspace: when the interaction energy between Rydberg states is much larger than the Rabi strength, the exact dynamics in the full Hilbert space is well approximated by the dynamics in the subspace where only one Rydberg excitation is allowed between nearby atoms [39]. In numerical simulations, the states $|11\rangle_{ij}$ are therefore ignored if the distance between i and j is smaller than a given subspace radius R_s , which results in much faster computations. The default setting in most programs is $R_s = R_b$, so the quantum evolution is restricted to the independent sets in unit disk graphs. However, this approximation is too coarse to get accurate results—see Fig. 15: ignoring the states $|11\rangle$ for next-nearest neighbors (extremities of a diagonal) leads to success probabilities that are overestimated by up to 50%. Therefore, it is crucial to simulate either the full Hilbert space or the blockade subspace where only nearest-neighbor Rydberg states are ignored.

b. Optimization algorithm

In this study, we focus on the probability of reaching a MIS, i.e., we want to maximize the overlap between the quantum state at the end of the evolution and all MIS solutions of the graph under investigation; see Eq. (4). The set of parameters Θ to be optimized depends on the protocol, e.g., $\Theta = (\tau_i, \tau_f, \Delta_i, \Delta_f)$ for the simple linear schedules. Since the Schrödinger evolution is deterministic and we simulate noiseless systems, any standard optimization algorithm may be applied. We choose the simplex search method [53], which turns out to be robust and very efficient in our setting. Finally, we set $t_f = 1\text{ ps}$, which leads to success probabilities that are well distributed over the whole unit interval for the 500 graphs of the dataset.

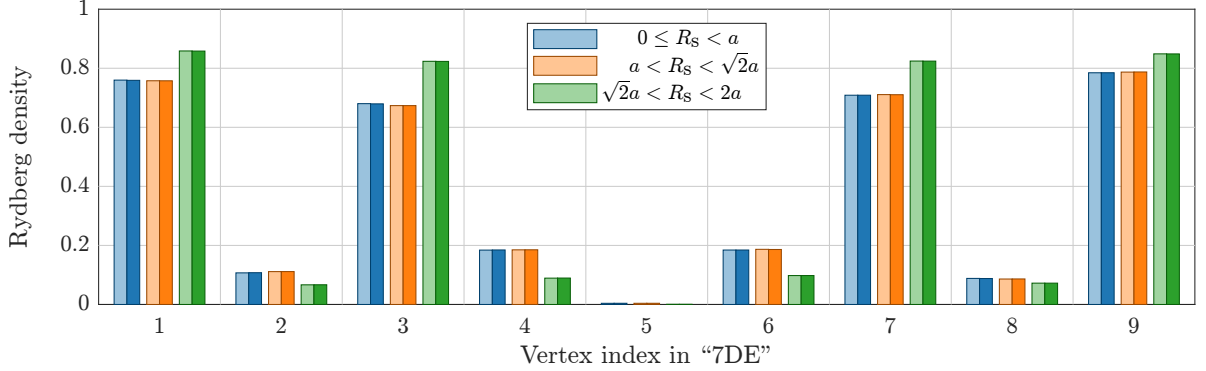


FIG. 15. Numerical simulations of the Rydberg Hamiltonian for the toy graph “7DE” and the ACQC protocol defined in Ref. [32] with $t_f = 1 \mu\text{s}$. The height of the bars represents the probability to find the atom i in the state $|1\rangle$ at the end of the evolution, with $i = 1, \dots, 9$ from top to bottom and left to right in the graph. The MIS solution (1, 3, 7, 9) is clearly visible in this bar chart. We verify that our implementation (light colors) is perfectly equivalent to that of **BLOQUADE** (dark colors); note that, depending on the software development kit, the phase has to be multiplied by minus one in Eq. (B9b). We also observe that the simulations in the full Hilbert space (blue bars) match those performed in the blockade subspace of nearest neighbors (orange bars). However, the unit disk subspace approximation $R_s = R_b$ (green bars) is clearly in favor of the MIS solution and thus cannot be considered as satisfactory. This is even more noticeable when comparing the probability to reach the ground state at the end of the evolution for each blockade subspace: 0.49(4), 0.49(6), and 0.70(0) respectively.

[1] F. Bova, A. Goldfarb, and R. G. Melko, Commercial applications of quantum computing, *EPJ Quantum Technology* **8**, 2 (2021).

[2] R. Au-Yeung, N. Chancellor, and P. Halffmann, NP-hard but no longer hard to solve? Using quantum computing to tackle optimization problems, *Frontiers in Quantum Science and Technology* **2**, 10.3389/frqst.2023.1128576 (2023).

[3] A. Abbas, A. Ambainis, B. Augustino, A. Bärtschi, H. Buhrman, C. Coffrin, G. Cortiana, V. Dunjko, D. J. Egger, B. G. Elmegreen, N. Franco, F. Fratini, B. Fuller, J. Gacon, C. Gonciulea, S. Gribling, S. Gupta, S. Hadfield, R. Heese, G. Kircher, T. Kleinert, T. Koch, G. Korpas, S. Lenk, J. Marecek, V. Markov, G. Mazzola, S. Mensa, N. Mohseni, G. Nannicini, C. O'Meara, E. P. Tapia, S. Pokutta, M. Proissl, P. Rebentrost, E. Sahin, B. C. B. Symons, S. Tornow, V. Valls, S. Woerner, M. L. Wolf-Bauwens, J. Yard, S. Yarkoni, D. Zechiel, S. Zhuk, and C. Zoufal, Challenges and opportunities in quantum optimization, *Nature Reviews Physics* **6**, 718 (2024).

[4] E. Farhi, J. Goldstone, S. Gutmann, J. Lapan, A. Lundgren, and D. Predu, A quantum adiabatic evolution algorithm applied to random instances of an NP-complete problem, *Science* **292**, 472 (2001).

[5] A. Lucas, Ising formulations of many NP problems, *Frontiers in Physics* **2**, 10.3389/fphy.2014.00005 (2014).

[6] T. Albash and D. A. Lidar, Adiabatic quantum computation, *Rev. Mod. Phys.* **90**, 015002 (2018).

[7] E. K. Grant and T. S. Humble, Adiabatic quantum computing and quantum annealing (2020).

[8] A. del Campo, Shortcuts to adiabaticity by counterdiabatic driving, *Phys. Rev. Lett.* **111**, 100502 (2013).

[9] M. Ohkuwa, H. Nishimori, and D. A. Lidar, Reverse annealing for the fully connected p -spin model, *Phys. Rev. A* **98**, 022314 (2018).

[10] E. J. Crosson and D. A. Lidar, Prospects for quantum enhancement with diabatic quantum annealing, *Nature Reviews Physics* **3**, 466 (2021).

[11] B. F. Schiffer, J. Tura, and J. I. Cirac, Adiabatic spectroscopy and a variational quantum adiabatic algorithm, *PRX Quantum* **3**, 020347 (2022).

[12] J. Wurtz, P. L. S. Lopes, C. Gorgulla, N. Gemelke, A. Keesling, and S. Wang, Industry applications of neutral-atom quantum computing solving independent set problems (2024), arXiv:2205.08500 [quant-ph].

[13] V. Boginski, S. Butenko, and P. M. Pardalos, Statistical analysis of financial networks, *Computational Statistics & Data Analysis* **48**, 431 (2005).

[14] R. M. Karp, Reducibility among combinatorial problems, in *Complexity of Computer Computations: Proceedings of a symposium on the Complexity of Computer Computations, held March 20–22, 1972, at the IBM Thomas J. Watson Research Center, Yorktown Heights, New York, and sponsored by the Office of Naval Research, Mathematics Program, IBM World Trade Corporation, and the IBM Research Mathematical Sciences Department*, edited by R. E. Miller, J. W. Thatcher, and J. D. Bohlinger (Springer US, Boston, MA, 1972) pp. 85–103.

[15] B. N. Clark, C. J. Colbourn, and D. S. Johnson, Unit disk graphs, *Discrete Mathematics* **86**, 165 (1990).

[16] R. S. Andrist, M. J. A. Schuetz, P. Minssen, R. Yalovetzky, S. Chakrabarti, D. Herman, N. Kumar, G. Salton, R. Shaydulin, Y. Sun, M. Pistoia, and H. G. Katzgraber, Hardness of the maximum-independent-set problem on unit-disk graphs and prospects for quantum speedups, *Phys. Rev. Res.* **5**, 043277 (2023).

[17] H. Pichler, S.-T. Wang, L. Zhou, S. Choi, and M. D. Lukin, Quantum optimization for maximum independent set using rydberg atom arrays (2018), arXiv:1808.10816 [quant-ph].

[18] L. Henriet, L. Beguin, A. Signoles, T. Lahaye, A. Browaeys, G.-O. Reymond, and C. Jureczak, Quantum computing with neutral atoms, *Quantum* **4**, 327 (2020).

[19] S. Ebadi, A. Keesling, M. Cain, T. T. Wang, H. Levine, D. Bluvstein, G. Semeghini, A. Omran, J.-G. Liu, R. Samajdar, X.-Z. Luo, B. Nash, X. Gao, B. Barak, E. Farhi, S. Sachdev, N. Gemelke, L. Zhou, S. Choi, H. Pichler, S.-T. Wang, M. Greiner, V. Vuletić, and M. D. Lukin, Quantum optimization of maximum independent set using rydberg atom arrays, *Science* **376**, 1209 (2022).

[20] M. Cain, S. Chattopadhyay, J.-G. Liu, R. Samajdar, H. Pichler, and M. D. Lukin, Quantum speedup for combinatorial optimization with flat energy landscapes (2023), arXiv:2306.13123 [quant-ph].

[21] C. Dalyac, L.-P. Henry, M. Kim, J. Ahn, and L. Henriet, Exploring the impact of graph locality for the resolution of the maximum-independent-set problem with neutral atom devices, *Phys. Rev. A* **108**, 052423 (2023).

[22] B. F. Schiffer, D. S. Wild, N. Maskara, M. Cain, M. D. Lukin, and R. Samajdar, Circumventing superexponential runtimes for hard instances of quantum adiabatic optimization, *Phys. Rev. Res.* **6**, 013271 (2024).

[23] M. J. A. Schuetz, R. S. Andrist, G. Salton, R. Yalovetzky, R. Raymond, Y. Sun, A. Acharya, S. Chakrabarti, M. Pistoia, and H. G. Katzgraber, Quantum compilation toolkit for rydberg atom arrays with implications for problem hardness and quantum speedups (2024), arXiv:2412.14976 [quant-ph].

[24] M. D. Lukin, M. Fleischhauer, R. Cote, L. M. Duan, D. Jaksch, J. I. Cirac, and P. Zoller, Dipole blockade and quantum information processing in mesoscopic atomic ensembles, *Phys. Rev. Lett.* **87**, 037901 (2001).

[25] J. Wurtz, A. Bylinskii, B. Braverman, J. Amato-Grill, S. H. Cantu, F. Huber, A. Lukin, F. Liu, P. Weinberg, J. Long, S.-T. Wang, N. Gemelke, and A. Keesling, Aquila: Quera's 256-qubit neutral-atom quantum computer (2023), arXiv:2306.11727 [quant-ph].

[26] E. Farhi, J. Goldstone, and S. Gutmann, A quantum approximate optimization algorithm (2014), arXiv:1411.4028 [quant-ph].

[27] N. Moll, P. Barkoutsos, L. S. Bishop, J. M. Chow, A. Cross, D. J. Egger, S. Filipp, A. Fuhrer, J. M. Gambetta, M. Ganzhorn, A. Kandala, A. Mezzacapo, P. Müller, W. Riess, G. Salis, J. Smolin, I. Tavernelli, and K. Temme, Quantum optimization using variational algorithms on near-term quantum devices, *Quantum Science and Technology* **3**, 030503 (2018).

[28] M. Cerezo, A. Arrasmith, R. Babbush, S. C. Benjamin, S. Endo, K. Fujii, J. R. McClean, K. Mitarai, X. Yuan, L. Cincio, and P. J. Coles, Variational quantum algo-

rithms, *Nature Reviews Physics* **3**, 625 (2021).

[29] M. Demirplak and S. A. Rice, Adiabatic population transfer with control fields, *The Journal of Physical Chemistry A* **107**, 9937 (2003).

[30] M. V. Berry, Transitionless quantum driving, *Journal of Physics A: Mathematical and Theoretical* **42**, 365303 (2009).

[31] D. Sels and A. Polkovnikov, Minimizing irreversible losses in quantum systems by local counterdiabatic driving, *Proceedings of the National Academy of Sciences* **114**, E3909 (2017).

[32] Q. Zhang, N. N. Hegade, A. G. Cadavid, L. Lassablière, J. Trautmann, S. Perseguers, E. Solano, L. Henriet, and E. Michon, Analog counterdiabatic quantum computing (2024), arXiv:2405.14829 [quant-ph].

[33] J. R. Finžgar, M. J. A. Schuetz, J. K. Brubaker, H. Nishimori, and H. G. Katzgraber, Designing quantum annealing schedules using Bayesian optimization, *Phys. Rev. Res.* **6**, 023063 (2024).

[34] J. R. Finžgar, A. Kerschbaumer, M. J. Schuetz, C. B. Mendl, and H. G. Katzgraber, Quantum-informed recursive optimization algorithms, *PRX Quantum* **5**, 020327 (2024).

[35] W. da Silva Coelho, M. D’Arcangelo, and L.-P. Henry, Efficient protocol for solving combinatorial graph problems on neutral-atom quantum processors (2022), arXiv:2207.13030 [quant-ph].

[36] J. Wurtz, S. Sack, and S.-T. Wang, Solving nonnative combinatorial optimization problems using hybrid quantum-classical algorithms, *IEEE Transactions on Quantum Engineering* **5**, 1 (2024).

[37] X. Ge, R.-B. Wu, and H. Rabitz, The optimization landscape of hybrid quantum-classical algorithms: From quantum control to nisq applications, *Annual Reviews in Control* **54**, 314 (2022).

[38] We equally refer to the number of vertices in a graph as *order* or *size*. In quantum computing, the latter is commonly understood as the size of the system and not as the number of edges in the graph (mathematical definition).

[39] QuEra Computing, Tutorials: Rydberg blockade, <https://queracomputing.github.io/Bloqade.jl/stable/tutorials/1.blockade/main/>, accessed: 2025-03-19.

[40] Amazon Web Services, Quantum computing with neutral atoms, <https://aws.amazon.com/braket/> quantum-computers/quera/, accessed: 2024-09-25.

[41] H. Silvério, S. Grijalva, C. Dalyac, L. Leclerc, P. J. Karalekas, N. Shammah, M. Beji, L.-P. Henry, and L. Henriet, Pulser: An open-source package for the design of pulse sequences in programmable neutral-atom arrays, *Quantum* **6**, 629 (2022).

[42] L. Leclerc, *Quantum computing with Rydberg atoms : control and modelling for quantum simulation and practical algorithms*, Ph.D. thesis, Université Paris-Saclay (2024).

[43] K. Kim, M. Kim, J. Park, A. Byun, and J. Ahn, Quantum computing dataset of maximum independent set problem on king lattice of over hundred rydberg atoms, *Scientific Data* **11**, 111 (2024).

[44] D. Guéry-Odelin, A. Ruschhaupt, A. Kiely, E. Torrontegui, S. Martínez-Garaot, and J. G. Muga, Shortcuts to adiabaticity: Concepts, methods, and applications, *Rev. Mod. Phys.* **91**, 045001 (2019).

[45] J.-G. Liu, L. Wang, and P. Zhang, Tropical tensor network for ground states of spin glasses, *Phys. Rev. Lett.* **126**, 090506 (2021).

[46] J.-G. Liu, X. Gao, M. Cain, M. D. Lukin, and S.-T. Wang, Computing solution space properties of combinatorial optimization problems via generic tensor networks, *SIAM Journal on Scientific Computing* **45**, A1239 (2023).

[47] R. Orús, Tensor networks for complex quantum systems, *Nature Reviews Physics* **1**, 538 (2019).

[48] S. Perseguers, GitHub repository of Gradiom Sàrl, <https://github.com/Gradiom/quantum/> (2024).

[49] E. Boros and P. L. Hammer, Pseudo-boolean optimization, *Discrete Applied Mathematics* **123**, 155 (2002).

[50] V. Choi, Minor-embedding in adiabatic quantum computation: I. the parameter setting problem, *Quantum Information Processing* **7**, 193 (2008).

[51] P. Weinberg, K.-H. Wu, J. Long, and X.-z. R. Luo, Queracomputing/bloqade-python: v0.15.11 (2024).

[52] P. Bogacki and L. Shampine, A 3(2) pair of Runge–Kutta formulas, *Applied Mathematics Letters* **2**, 321 (1989).

[53] J. C. Lagarias, J. A. Reeds, M. H. Wright, and P. E. Wright, Convergence properties of the Nelder–Mead simplex method in low dimensions, *SIAM J. Optim.* **9**, 112 (1998).